Weakening of Ice by Magnesium Perchlorate Hydrate

by

Hendrik J. Lenferink

B.S. with Highest Honors, University of Maine, 2008

SUBMITTED TO THE DEPARTMENT OF EARTH, ATMOSPHERIC AND PLANETARY SCIENCES
IN PARTIAL FULFILLMENT OF THE REQUIREMENTS FOR THE DEGREE OF

MASTER OF SCIENCE IN GEOPHYSICS
AT THE
MASSACHUSETTS INSTITUTE OF TECHNOLOGY

SEPTEMBER 2012

Signature of author: _____
Department of Earth, Atmospheric and Planetary Sciences
August 27, 2012

Certified by: _____
William B. Durham
Senior Research Scientist
Thesis Supervisor

Accepted by: _____
Robert D. van der Hilst
Schlumberger Professor of Earth Sciences
Head, Department of Earth, Atmospheric and Planetary Sciences

Weakening of Ice by Magnesium Perchlorate Hydrate

by

Hendrik J. Lenferink

B.S. with Highest Honors, University of Maine, 2008

SUBMITTED TO THE DEPARTMENT OF EARTH, ATMOSPHERIC AND PLANETARY SCIENCES
IN PARTIAL FULFILLMENT OF THE REQUIREMENTS FOR THE DEGREE OF

MASTER OF SCIENCE IN GEOPHYSICS
AT THE
MASSACHUSETTS INSTITUTE OF TECHNOLOGY

SEPTEMBER 2012

Abstract

I show that perchlorate hydrates, which have been indirectly detected at high Martian circumpolar latitudes by the Phoenix Mars Lander, have a dramatic effect upon the rheological behavior of polycrystalline water ice under conditions applicable to the north polar layered deposits (NPLD). I conducted subsolidus creep tests on mixtures of ice and magnesium perchlorate hexahydrate (MP6) of 0.02, 0.05, 0.10, and 0.47 volume fraction MP6. I found these mixtures to be increasingly weak with increasing MP6 content. For mixtures with ≤ 0.10 volume fraction MP6, I resolved a stress exponent of $n \approx 2$ at low stresses transitioning to $n \approx 4$ above 10 MPa. Scanning electron microscopy of deformed specimens revealed MP6 to be distributed as an interconnected film between ice grains. These results suggest that grain boundary sliding (GBS) may be enhanced with respect to pure ice. As the enhancement of GBS is expected in polycrystalline aggregates containing a few percent melt or otherwise weak material distributed along grain boundaries, the observed $n \approx 2$ is consistent with the mutual accommodation of basal slip and GBS. If ice containing trace concentrations of MP6 is also much weaker than pure ice at low stresses, flow in the NPLD could be significantly enhanced, particularly at the warmer basal temperatures associated with higher Martian obliquities.

Thesis Supervisor: William B. Durham
Title: Senior Research Scientist

Table of Contents

Introduction

The Phoenix Mars Lander detected 0.4–0.6% perchlorate by mass in Martian soils located at high northern latitudes (Figure 1) (Hecht et al., 2009). Considering the ubiquity of terrestrial perchlorate (ClO_4^-) within the Antarctic Dry Valleys (Kounaves et al., 2010), perchlorate is likely also to be widespread in the Martian polar regions. If the north polar layered deposits (NPLD)—the largest surface reservoir of water ice on Mars—contain a few percent dust (Langevin et al., 2005) with a perchlorate component similar to that observed at the Phoenix landing site, the effect of this phase may be sufficient to enhance flow rates in the NPLD. For example, Fisher et al. (2010) suggest that a perchlorate brine in basal layers could indirectly facilitate flow in the overlying NPLD. In this work, I investigate the rheological effects of perchlorate upon polycrystalline ices deforming at Martian polar temperatures by direct experiments.

The ice plus magnesium perchlorate ($Mg(ClO_4)_2$) system is of particular interest. This system has a eutectic melting temperature (T_e) of 206 K at 56 wt.% H_2O (Figure 2), where the two phases are ice I and magnesium perchlorate hexahydrate ($Mg(ClO_4)_2 \cdot 6H_2O$; referred to hereafter as "MP6") (Chevrier et al., 2009; Pestova et al., 2005). More recently, Stillman and Grimm (2011a) reported T_e = 216 K based on dielectric permittivity measurements. Although various salts and salt hydrates may be present at the Phoenix landing site, the predominant form of perchlorate should be MP6, based on its stability at low temperatures (Robertson and Bish, 2011).

At near-eutectic temperatures, mixtures of ice and MP6 should be weaker than the individual end-member phases. There are clear examples of this behavior in subsolidus mixtures of ice and NaCl (De La Chapelle et al., 1995; 1999). The weakening effect in

the ice-MP6 system may be especially pronounced, given that the difference between the eutectic temperature and melting temperatures of the end-member phases is so large (Figure 1).

To test this hypothesis and quantify the effect, I conducted a series of deformation experiments on ice containing various concentrations of MP6. I found these mixtures to be increasingly weak with increasing MP6 content. For mixtures with ≤ 0.10 volume fraction MP6, I resolved a stress exponent of $n \approx 2$ at low stresses transitioning to $n \approx 4$ above 10 MPa. Examination of deformed specimens in a scanning electron microscope revealed an interconnected MP6-rich film between ice grains. Combined, these results suggest that grain boundary sliding (GBS) may be enhanced with respect to pure ice, owing to localized shear in MP6-rich regions. Extrapolating to low stresses and trace concentrations of MP6, I conclude that flow in the NPLD could be significant over Ma timescales.

Flow of Icy Systems Exhibiting a Eutectic

Steady-state rheological behavior can be described by the constitutive relationship (*e.g.*, *Poirier* (1985))

$$\dot{\varepsilon} = A\,\sigma^{n} d^{-p} \exp\left(-\frac{E^{*} + PV^{*}}{RT}\right) . \qquad (1)$$

Here $\dot{\varepsilon}$ is strain rate, σ is differential stress (simply referred to as stress), d is grain size, P is pressure, T is temperature, R is the universal gas constant, and A, n, p, E^{*}, and V^{*} are constants specific to the material and to the deformation mechanism.

Several deformation mechanisms have been observed in pure polycrystalline ice (Table 1). Figure 3 depicts the manner in which various ice creep mechanisms contribute to bulk strain rate. Deformation in the laboratory of pure, coarse-grained ice at geological (and faster-than-geological) strain rates is ordinarily rate-limited by dislocation creep, with grains changing shape through intracrystalline plasticity and accompanied by recrystallization. For ice at Martian temperatures, grain size-sensitive mechanisms such as diffusional flow and grain boundary sliding (GBS) play an increasing role at low stresses. Diffusional flow, both within grain interiors as well as along grain boundaries, is expected on a theoretical basis (Goodman et al., 1981); it is plausibly manifested in low-stress geological settings but has not yet been observed in ice in the laboratory.

Secondary phases introduce a complexity to deformation that depends not only on the volume fractions and constitutive relationships of those phases, but also their spatial distribution within and chemical reactivity with the primary phase. The effect on ice flow behavior of inert materials such as hard particulates is well understood at high and low temperatures (Baker and Gerberich, 1979; Durham et al., 1992; Durham et al., 2009; Hooke et al., 1972; Mangold et al., 2002). However, systems of ice and secondary phases exhibiting a eutectic are far less predictable, owing to weak heterophase interfaces (at $T \lesssim T_e$) and the presence of a melt phase ($T > T_e$) that may enhance grain boundary processes.

Creep tests on partially molten aggregates of saline ice by De La Chapelle et al. (1995; 1999) revealed low $n = 1.8 \pm 0.2$ behavior in the low-stress portion of the known dislocation creep regime of pure ice (Figure 4)—consistent with an enhanced rate of GBS. Hirth and Kohlstedt (1995a; 1995b) observed similar weakening in partially molten dunites, and postulated that grain boundary diffusion and GBS were contributing more to

deformation than activity of the stronger slip systems of olivine.

The enhancement of grain boundary processes in eutectic mixtures is expected at slightly subsolidus temperatures as well. McCarthy et al. (2011) found fine-scale ice-meridianiite ($MgSO_4 \cdot 11H_2O$) eutectic intergrowths to manifest a "colony boundary sliding" mechanism analogous to GBS in the range $0.85 < T/T_e < 0.93$. In general, though, creep tests of ice-rich eutectic systems at subsolidus temperatures have not suggested enhancement of grain boundary processes, as most have been performed at relatively high stresses (De La Chapelle et al., 1995; 1999; Durham et al., 1993; Durham et al., 2005).

Experimental Methods

Specimen material of various compositions was fabricated by mixing measured amounts of granular ice (coarse-grained, $180 < d < 250$ μm; and in one case fine-grained, $2 < d < 5$ μm) with powdered eutectic ice-MP6. The eutectic mixture itself was made by dissolving anhydrous $Mg(ClO_4)_2$ in water at a H_2O:$Mg(ClO_4)_2$ mass ratio of 56:44 (refer to Figure 1), then cooling below T_e. X-ray diffraction (XRD) demonstrated that upon first cooling the solid is highly non-crystalline; it is also rather soft, with a consistency at 190–200 K of modeling clay. If T is cycled above and below T_e, the material devitrifies dramatically, and with continued agitation becomes much harder. At this stage the material is sufficiently brittle that it can be pulverized for the purpose of specimen fabrication. When the T-cycled material is further pressurized above 100 MPa, it becomes completely crystalline, within the resolution limits of XRD. Figure 5 shows cryogenic scanning electron microscope images of an ice-MP6 eutectic that I deformed at high

pressure (run 603). The eutectic solid has a texture that is fairly typical of other eutectics, displaying interfingering of extended zones of ice and MP6 (as discussed below in the "Microstructural Observations" subsection).

Compressional creep tests ("runs") on composite specimens of ice and MP6 were performed under elevated confining pressure in the gas-medium, cryogenic triaxial deformation apparatus described by Durham et al. (1983). Cylindrical specimens approximately 25 mm in diameter and 60 mm in length were prepared by spooning mixed powders of desired composition into indium tubes, tamping to remove large pores, then sealing the tubes to end plugs. All handing and storage was at 180 K or colder. Upon entering the deformation apparatus and equilibrating to a temperature of 190 K, the specimen was pressurized hydrostatically to 150 MPa for two reasons: to assure complete crystallinity, and to squeeze out all specimen porosity that would otherwise interfere with the mechanical response to the applied stress. Figure 6 shows the progress of compaction with confining pressure resulting from the loss of pore space.

Runs consisted of deformation steps at various stress and temperature conditions, and were all performed at a gas confining pressure of 50 MPa. An example of a step test is shown in Figure 7, and deformed specimens in Figures 8 and 9. Specimens were shortened by a total of 10–30% over a period of hours to days, depending on conditions. The step testing technique has the advantage of yielding several data points per run, but the disadvantage of potentially overlooking subtle but important strain-dependent effects. The immediate strain rate response to a change in environmental conditions at the beginning of a step is usually transient (i.e., strain-dependent). For stress increases following a step change, the transient strain rate is higher than the strain rate later in the

step. Once the specimen appears to exhibit approximately steady-state behavior (after 1–2% strain at low stresses; 4–5% at high stresses), the current strain rate becomes the measured stress at that step. For the purposes of a reconnaissance investigation I assume that further strain dependence does not exist—an assumption that must eventually be confirmed by experiment.

Cryogenic scanning electron microscopy (CSEM) was used to observe the grain sizes and phase distribution of all specimens in this study. Specimens were shipped and prepared for CSEM at $T < 85$ K, then transferred to a cryogenic preparation station (Gatan Alto 2100) in which each specimen was cleaved under vacuum to produce fresh surfaces uncontaminated by water condensation. Specimens were then transferred directly into a LEO 982 field-emission SEM equipped with a cryogenic stage. A thermocouple embedded in the SEM specimen stage monitored temperature throughout the imaging process. Images were taken at $T < 85$ K and vacuum below 10^{-5} mbar.

Results and Analysis

Creep Results

Experimental conditions and results are given in Table 2. I tested nine specimens of MP6 volume fractions of 0 to 0.47 at $180 \leq T \leq 210$ K in stepped tests that yielded 34 data points. One of the nine specimens (639) was a stacked assembly designed for a comparative measurement of $\chi_{MP6} = 0.02$ ice and pure ice (Figure 9). As stated in the previous section, the ice component in one of the mixtures (657) was fine- rather than coarse-grained. After discovering a strong effect of MP6 on strength, and after seeing

signs of partial melting at 210 K (see "Partial Melting" subsection below), I concentrated mainly on lower temperatures of ~200 K and MP6 concentrations $\chi_{MP6} \leq 0.10$.

Of the 34 data points, 26 are plotted in Figure 10 along with temperature contours for the creep of polycrystalline ice of various grain sizes (5, 30, and 200 μm) (Goldsby and Kohlstedt, 2001). The effect of MP6 on the ductile strength of ice is profound. All specimens were weaker than pure, coarse-grained ice at the same stress and temperature conditions. At 180 K, the observed strain rate of the eutectic alloy $\chi_e = 0.47$ was nearly 1.5 orders of magnitude faster than pure ice at the same stress, and at 195 K the strain rate contrast was well over 10^3. For specimens of $\chi_{MP6} \leq 0.10$, Figure 10 shows two distinct flow regimes: above 10 MPa, log strain rate vs. log stress for a given concentration and temperature follows a trend with slope $n \approx 4$ (refer to Equation 1), paralleling that of pure, coarse-grained ice. Below 10 MPa, the data follow more closely the $n \approx 2$ trend seen in pure, fine-grained ice (Goldsby and Kohlstedt, 1997; 2001).

The effect of MP6 concentration on strength may be more pronounced in the $n \approx 4$ regime than in the $n \approx 2$ regime: there is a relatively small spread among the data as they transition with decreasing stress from the high to the low n regime. It is not surprising that the one mixture containing fine-grained ice (open triangles in Figure 10) follows the trend for pure ice with $d = 5$ μm, as this is the expected behavior. What is remarkable, though, is that coarse-grained ice containing a relatively small amount of MP6 behaves rheologically like fine-grained ice. Like pure, fine-grained ice, the behavior of this group of specimens demonstrates a rheological similarity to basal slip in monocrystalline ice: it not only exhibits a strength in this same general region, but like basal slip it is also insensitive to grain size. This point is discussed in more detail below.

The data viewed as strain rate vs. χ_{MP6} at constant stress and temperature show more clearly the magnitude of the weakening effect of MP6 (Figure 11). Data are sparse and somewhat scattered, but for the most part consistently indicate that the profound weakening near χ_e continues to very low χ_{MP6}. The best resolved measurement is that of the stacked assembly run 639, conducted at 190 K, which showed on the basis of comparative shape change a strain rate enhancement in the $\chi_{MP6} = 0.02$ sub-specimen with respect to the pure ice sub-specimen by a factor of 1.16 ± 0.04. Evidently, the enhancement should increase with temperature above 190 K, and if the estimated trends in Figure 11 correctly characterize the behavior, it should still be significant even for $\chi_{MP6} < 0.01$.

Partial Melting

The two specimens deformed at 210 K show almost unmistakable signs of having partially melted. Firstly, they exhibited a drop in strength between 200 and 210 K that was anomalously high given the temperature sensitivity of the of MP6 mixtures (and of pure ice) at lower temperatures. Secondly, and more convincingly, both these specimens lost volume during the experiments. External dimensions indicated a volume loss of ~1%, and a rigid ~1 cm^3 internal plenum—which ordinarily remains empty during a deformation test—was filled with material that in one case was confirmed by density measurement to be of eutectic composition. (The plenum communicates gas pressure with the specimen through an axial hole 0.5 mm in diameter by 20 mm in length, and is vented to the atmosphere through a much finer axial hole in the force gauge.)

I cannot say at this point how much material escaped through the vent hole, or if the

Clapeyron slope for eutectic melting is sufficiently negative that material resolidified upon entering the plenum at test conditions. In any case, the material in the plenum was solid when viewed because the specimen assembly cooled to 77 K before it was taken apart. The Clapeyron slope for the melting of ice I is approximately 10 MPa/K; if this value has any relationship to the value for eutectic melting, then given the 50-MPa pressure drop between the specimen and plenum, my observation of melt formation at 210 K does not better constrain the $P = 0$ melting point relative to published work (Chevrier et al., 2009; Pestova et al., 2005; Stillman and Grimm, 2011b).

Microstructural Observations

Sections from all specimens were observed by CSEM. The specimen of eutectic composition $\chi_{MP6} = 0.47$ (Figure 5) exhibits many regions with classic eutectic solidification microstructures similar to those described by McCarthy et al. (2007) in which the hydrate phase forms a matrix around regularly spaced rods of ice I. Also similar to the McCarthy et al. (2007) study was the observation of rapid sublimation of the ice phase in all specimens, in contrast to the behavior of pure ice specimens that sublimate very slowly in the FESEM at comparable conditions. The sublimation effect is illustrated in the right-hand panels of Figure 5, which span a 20-minute interval.

Figures 12, 13, and 14 show images from specimens of $\chi_{MP6} = 0.10$, 0.05, and 0.02, respectively. The general appearance of ice grains rimmed by MP6-rich material was consistently found throughout all the specimens, demonstrating the excellent reproducibility of phase distribution here that in turn supports comparison of creep results. In the absence of rigorous microanalysis of individual grains in these specimens, I

assume that the ice grains have little or no MP6 in their interiors, and that the intergranular phase is MP6-rich—close inspection of SEM images supports this assumption. While much of the MP6-rich material appears pitted and/or riddled with small cracks, these features are mainly an artifact of the high-vacuum conditions in the SEM.

For the $\chi_{MP6} = 0.10$ and 0.05 specimens (Figures 12 and 13), the coating of ice grains by MP6-rich material is complete—there are few if any direct grain-to-grain ice contacts. Distribution of MP6 in the $\chi_{MP6} = 0.02$ is sometimes more heterogeneous, although it still typically surrounds the ice grains (Figure 14). At this point, I cannot rule out the possibility that the heterogeneity is a mixing problem, so it is difficult to comment on rheological effects. Nonetheless, the similarity in overall phase distribution of the $\chi_{MP6} = 0.02$ specimens in Figure 14 (643 vs. 657) is striking: both show 100–300 μm diameter grains or domains of ice, even though those in 657 are domains composed of fine-grained ice rather than larger single grains.

The fine-grained $\chi_{MP6} = 0.02$ specimen (657) gives tantalizing clues about the kinetics of textural equilibration. Evidently, the preponderance of the MP6 in this specimen is along the domain boundaries, but on close examination of Figure 14b, one sees a fine network extending from the domain boundaries a few tens of microns' distance into the domains. The system is presumably evolving in the direction of textural equilibrium, with MP6-rich material moving from the domain boundaries to coat the boundaries between individual ice grains. Figure 15 shows closer views of these edges of the ice domain that support this interpretation.

Similarities in geologically relevant materials to the microstructures seen here include

the texture of interstitial fluids (H_2O, CO_2, partial melts) in polycrystalline rocks for which the dihedral angle (θ) between fluid and matrix is very low (Figure 16) (Ketcham and Hobbs, 1969; Lee et al., 1991; Kohlstedt, 2002). If the textural control of the MP6-rich grain boundary phase in my specimens is analogous, then given its propensity to completely surround ice grains even at low volume fractions, the dihedral angle must be nearly zero. Furthermore, given that MP6 is in fact a crystalline solid and should not penetrate between grains as rapidly as a fluid, there is reason to suspect that chemical processes play a more significant role than do capillary forces in the textural equilibration of my specimens.

Discussion

Although this investigation is preliminary, two observations are especially noteworthy: a profound mechanical weakening associated with the presence of small amounts of MP6, and a remarkable—considering that the material has been entirely below T_e—texture of ice grains surrounded nearly or completely by MP6-rich material in deformed specimens. The coincidence of the two invites speculation about a causal relationship. If such a relationship exists, the distribution of the MP6-rich material suggests a weakening associated with strain rate localization in MP6-rich regions. The MP6-rich material may act in some way to weaken the connection between adjacent ice grains, either via (1) normal displacement, by removing contact points in the manner of pressure solution, and (2) shear displacement, by decreasing the shear stress between flat surfaces or by smoothing asperities between rough surfaces.

Diffusion creep tends to follow a linear stress-strain rate relationship and can

probably be eliminated as a rate-limiting mechanism. But the mutual accommodation of intergranular shear displacement (in the form of GBS) and intragranular plasticity could account for this weakening and explain the rheological similarity to pure, fine-grained ice. My creep results at $\sigma < 10$ MPa for $\chi_{MP6} = 0.05$ and 0.10 exhibit both the $n \approx 2$ dependence and level of strain rate of basal slip-limited creep, as seen in pure ice of $d < 5$ μm (Goldsby and Kohlstedt, 1997; 2001). Perhaps, then, the presence of the MP6-rich material allowed large ice grains to effectively act as if they were smaller.

The one grain size comparison I have, ~200 μm vs. ~5 μm at $\chi_{MP6} = 0.02$ and 200 K (runs 643 and 657), indicates a weak but non-zero grain-size dependence that may indicate a transition to GBS-limited creep at the conditions of the coarse-grained specimen 643. Here I must consider the possible effect of a fixed volume of MP6 available per unit volume: if the thickness of the grain boundary layer matters in some way, an increase in grain boundary area per unit volume—which enhances GBS in pure ice—may in turn be offset by the thinning of the grain boundary layer with decreasing grain size.

Implications for Ice Flow in the North Polar Layered Deposits

Whether or not the topography and stratigraphy of the NPLD (Figure 17) is consistent with past ice flow is currently a matter of debate. Winebrenner et al. (2008) analyzed the morphology of Gemina Lingula—a lobe of the NPLD—and demonstrated that its inter-trough topography (Figure 18) can be reproduced by glacial flow. Karlsson et al. (2011), however, proffer that the radar-detected subsurface stratigraphy of Gemina Lingula is inconsistent with the predictions of a flow model. In response, Winebrenner et al. (2012)

have shown that the stratigraphy of Gemina Lingula is not incompatible with a slope-dependent mass balance pattern, which they argue is more appropriate to the NPLD.

What is less contentious, though, is the widespread conclusion (Clifford et al., 2000; Greve and Mahajan, 2055; Hvidberg, 2003; Koutnik et al., 2012) that pure water ice at present-day NPLD thermal conditions (i.e., basal $T_b \approx 185$ K) is too viscous to undergo significant flow. Koutnik et al. (2012) suggest that both warmer basal temperatures and flow enhancement (by at least a factor of 10) may be required to generate significant flow over plausible time scales. If my laboratory results can be extrapolated to low stresses (< 0.1 MPa) and trace concentrations of MP6 (<< 1% by volume), the presence of perchlorate in the NPLD could account for such flow enhancement—particularly at slightly elevated basal temperatures ($190 < T_b < 210$ K). Such warming could potentially result from transient subsurface heating events or increased insolation at higher obliquities (Pathare and Paige, 2005). Moreover, if NPLD basal temperatures are elevated above the MP6 eutectic, then as Fisher et al. (2010) suggest, a perchlorate brine-lubricated bed may facilitate flow. A north polar flow hypothesis is therefore potentially plausible, and would be bolstered by the detection of perchlorate in the NPLD.

Conclusions

Mixtures of ice and MP6 are significantly weaker than pure ice at low stresses, and this weakening is most pronounced in material of eutectic composition. Specimens with $\chi_{MP6} = 0.05$ and 0.10 exhibited low $n \approx 2$ behavior at stresses below 10 MPa, coinciding with the basal slip-limited creep of very fine-grained ice ($d = 5$ μm). A specimen with $\chi_{MP6} = 0.02$ also exhibited low-n behavior at low stresses, coinciding with GBS-limited

creep of ice with $d = 30$ μm. These observations may imply a mechanistic equivalence to pure, fine-grained ice.

Based on this preliminary work, assumptions regarding flow in the NPLD should account for the weakening of ice by MP6 and the possibility of $n \approx 2$ behavior at Martian stresses (~0.05 MPa; Zwally and Saba, 1999). If the results of my experiments can be extrapolated to low stresses and MP6 concentrations, episodes of significant NPLD flow enhancement could be facilitated by the presence of MP6 at slightly elevated basal temperatures.

Future creep tests on ice-MP6 mixtures should be aimed at (1) determining the critical MP6 content required for significant weakening, and (2) probing for grain size-sensitive regimes (grain boundary diffusion- and sliding-limited creep).

Acknowledgments

I thank my supervisor, William B. Durham, for guiding my work; Laura A. Stern for facilitating CSEM and XRD analysis; Asmin V. Pathare for helpful insights regarding flow in the NPLD; Stephen H. Kirby for comments that helped improve this thesis; David E. Stillman (SWRI, Boulder, CO) for supplying an initial batch of eutectic ice-MP6; my family and friends for their ceaseless encouragement. This work was supported by NASA Mars Fundamental Research grant number NNX11AN37G and NASA Earth and Space Sciences Fellowship number NNX11AP34H.

References

Baker, R. W., and W. W. Gerberich (1979), The effect of crystal size and dispersed-solid inclusions on the activation energy for creep of ice, Journal of Glaciology, 24, 179–194.

Chevrier, V. F., Hanley, J., and T. S. Altheide (2009), Stability of perchlorate hydrates and their liquid solutions at the Phoenix landing site, Mars, Geophysical Research Letters, 36, L10202.

Clifford, S. M., and 52 others (2000), The state and future of Mars polar science and exploration, Icarus, 144, 210–242.

Cuffey, K. M., and W. S. B. Paterson (2010), The Physics of Glaciers, Fourth Edition, Academic Press, Amsterdam, 704 pp.

De La Chapelle, S., Duval, P., Baudelet, B. (1995), Compressive creep of polycrystalline ice containing a liquid phase, Scripta Metallurgica et Materialia, 33, 447-450.

De La Chapelle, S., Milsch, H., Castelnau, O., and P. Duval (1999), Compressive creep of ice containing a liquid intergranular phase: rate-controlling processes in the dislocation creep regime, Geophysical Research Letters, 26, 251–254.

Durham, W. B., H. C. Heard, and S. H. Kirby (1983), Experimental deformation of polycrystalline H_2O ice at high pressure and low temperature: Preliminary results, Proc. Lunar Planet. Sci. Conf. 14th, Part 1, Journal of Geophysical Research, 88, suppl., B377–B392.

Durham, W. B., Kirby, S. H., and L. A. Stern (1992), Effects of Dispersed Particulates on the Rheology of Water Ice at Planetary Conditions. Journal of Geophysical Research-Planets, 97, 20,883–20,897.

Durham, W. B., Kirby, S. H., and L. A. Stern (1993), Flow of ices in the ammonia-water system, Journal of Geophysical Research, 98, 17,667–17,682.

Durham, W. B., Kirby, S. H., and L. A. Stern (1997), Creep of water ices at planetary conditions: A compilation, Journal of Geophysical Research, 102, 16,293–16,302.

Durham, W. B., Pathare, A. V., Stem, L. A., and H. J. Lenferink (2009), Mobility of icy sand packs, with application to Martian permafrost, Geophysical Research Letters, 36, L23203.

Durham, W. B., Stern, L. A., Kubo, T., and S. H. Kirby (2005), Flow strength of highly hydrated Mg- and Na-sulfate hydrate salts, pure and in mixtures with water ice, with application to Europa, Journal of Geophysical Research-Planets, 110, E12010.

Duval, P., M. F. Ashby, and I. Anderman (1983), Rate-controlling processes in the creep of polycrystalline ice, Journal of Physical Chemistry, 87, 4,066–4,074.

Fisher, D. A., Hecht, M. H., Kounaves, S. P., and D. C. Catling (2010), A perchlorate brine lubricated deformable bed facilitating flow of the north polar cap of Mars: Possible mechanism for water table recharging, Journal of Geophysical Research-Planets, 115, E00E12.

Goldsby, D. L., and D. L. Kohlstedt (1997), Grain boundary sliding in fine-grained ice I, Scripta Materialia, 37, 1,399–1,406.

Goldsby, D. L., and D. L. Kohlstedt (2001), Superplastic deformation of ice: Experimental observations, Journal of Geophysical Research, 106, 11,017–11,030.

Goodman, D. J., H. J. Frost, and M. F. Ashby (1981), The plasticity of polycrystalline ice, Philosophical Magazine A, 43, 665–695.

Greve, R., and R. A. Mahajan (2005), Influence of ice rheology and dust content on the dynamics of the north-polar cap of Mars, Icarus, 174, 475–485.

Hecht, M. H., Kounaves, S. P., Quinn, R. C., West, S. J., Young, S. M. M., Ming, D. W., Catling, D. C., Clark, B. C., Boynton, W. V., Hoffman, J., DeFlores, L. P., Gospodinova, K., Kapit, J., and P. H. Smith (2009), Detection of perchlorate and the soluble chemistry of Martian soil at the Phoenix Lander site, Science, 325, 64–67.

Hirth, G., and D. L. Kohlstedt (1995), Experimental constraints on the dynamics of the partially molten upper mantle: Deformation in the diffusion creep regime, Journal of Geophysical Research-Solid Earth, 100, 1,981–2,001.

Hooke, R. L., Dahlin, B. B., and M. T. Kauper (1972). Creep of ice containing dispersed fine sand, Journal of Glaciology, 11, 327–336.

Hvidberg, C. S. (2003), Relationship between topography and flow in the north polar cap on Mars, Annals of Glaciology, vol. 37, pp. 363–369.

Karlsson, N. B., Holt, J. W., and R. C. A. Hindmarsh (2011), Testing for flow in the north polar layered deposits of Mars using radar stratigraphy and a simple 3D ice-flow model, Geophysical Research Letters, 38, L24204.

Ketcham, W. M., and P. V. Hobbs (1969), An experimental determination of the surface energies of ice, Philosophical Magazine, 19, 1,161–1,173.

Kohlstedt, D. L. (2002), Partial melting and deformation, In: Plastic Deformation of Minerals and Rocks, Karato, S., and H. R. Wenk (Eds.), Reviews in Mineralogy and Geochemistry, Mineralogical Society of America, pp. 121–135.

Kounaves, S. P., Stroble, S. T., Anderson, R. M., Moore, Q., Catling, D. C., Douglas, S., McKay, C. P., Ming, D. W., Smith, P. H., Tamppari, L. K., and A. P. Zent (2010), Discovery of natural perchlorate in the Antarctic Dry Valleys and its global implications, Environmental Science and Technology, 44, 2,360–2,364.

Koutnik, M. R., Waddington, E. D., Winebrenner, D. P., A. V. Pathare (2012). Response timescales for Martian ice masses and implications for ice flow on Mars, Icarus, in review.

Langevin, Y., Poulet, F., Bibring, J. P., B. Gondet (2005), Sulfates in the north polar region of Mars detected by OMEGA/Mars express, Science, 307, 1,584–1,586.

Lee, V. W., Mackwell, S. J., and S. L. Brantley (1991), The effect of fluid chemistry on wetting textures in novaculite, Journal of Geophysical Research, 96, 10,023–10,037.

Mangold, N., Allemand, P., Duval, P., Geraud, Y., P. Thomas (2002), Experimental and theoretical deformation of ice-rock mixtures: Implications on rheology and ice

content of Martian permafrost, Planetary and Space Science, 50, 385–401.

McCarthy, C., Cooper, R. F., Goldsby, D. L., Durham, W. B., and S. H. Kirby (2011), Transient and steady state creep response of ice I and magnesium sulfate hydrate eutectic aggregates, Journal of Geophysical Research-Planets, 116, E04007.

McCarthy, C., Cooper, R. F., Kirby, S. H., Rieck, K. D., and L. A. Stern (2007), Solidification and microstructures of binary ice-I/hydrate eutectic aggregates, American Mineralogist, 92, 1,550–1,560.

Pathare, A. V., and D. A. Paige (2005), The effects of martian orbital variations upon the sublimation and relaxation of north polar troughs and scarps, Icarus, 174, 419–443.

Pestova, O. N., Myund, L. A., Khripun, M. K., and A. V. Prigaro (2005), Polythermal study of the systems $M(ClO_4)_2$-H_2O (M^{2+} = Mg^{2+}, Ca^{2+}, Sr^{2+}, Ba^{2+}), Russian Journal of Applied Chemistry, 78, 409–413.

Poirier, J.-P. (1985), Creep of Crystals: High-Temperature Deformation Processes in Metals, Ceramics and Minerals, Cambridge University Press, New York, 260 pp.

Robertson, K., and D. Bish (2011), Stability of phases in the $Mg(ClO_4)_2 \cdot nH_2O$ system and implications for perchlorate occurrences on Mars, Journal of Geophysical Research, 116, E07006.

Stillman, D. E., and R. E. Grimm (2011a), Dielectric signatures of adsorbed and salty liquid water at the Phoenix landing site, Mars, Journal of Geophysical Research-Planets, 116, E09005.

Stillman, D. E., Grimm, R. E. (2011b), Heterogeneous adsorbed and salty liquid water at the Phoenix landing site, Mars, 42nd Lunar and Planetary Science Conference, Abstract #2578.

Winebrenner, D. P., Koutnik, M. R., Waddington, E. D., Pathare, A. V., Murray, B. C., Byrne, S., J. L. Bamber (2008), Evidence for ice flow prior to trough formation in the Martian north polar layered deposits, Icarus, 195, 90–105.

Winebrenner, D. P., Pathare, A. V., Waddington, E. D., and M. R. Koutnik (2012), Is the radar stratigraphy of Gemina Lingula compatible with a history of ice flow?, in preparation.

Zwally, H. J., and J. L. Saba (1999), Driving stresses in Mars polar ice caps and conditions for ice flow, Fifth International Conference on Mars, Abstract #6151.

Tables

Table 1 – Equation (1) parameters for creep mechanisms of ice I_h at various conditions

	log A^a	n	p	E^* (kJ/mol)	V^* (cm^3/mol)	source
Dislocation creep ($\sigma < 1$ MPa, $T < 263$ K)	5.5	3.0	0	60		Cuffey and Paterson (2010)
Dislocation creep ($\sigma < 1$ MPa, $T > 263$ K)	16.4	3.0	0	115		Cuffey and Paterson (2010)
Dislocation creep ($\sigma > 4$ MPa, $T < 240$ K)	5.1	4.0	0	61	–13	Durham et al. (1987; 1997)
Basal slip	7.7	2.4	0	60		Goldsby and Kohlstedt (1997; 2001)
GBS ($T < 255$ K)	–2.4	1.8	1.4	49		Goldsby and Kohlstedt (1997; 2001)
GBS ($T > 255$ K)	26.5	1.8	1.4	192		Goldsby and Kohlstedt (1997; 2001)

[a] for σ in MPa, d in μm

Table 2 – Experimental conditions and results

Run (step)	χ_{MP6}	T (K)	σ (MPa)	$\Delta\ell/\ell_0$	$\dot{\varepsilon}$ (s^{-1})
603(1)	0.47	180	18.0	0.026	5.26×10^{-7}
603(2)		190	5.5	0.070	1.14×10^{-6}
603(3)		195	3.0	0.110	2.00×10^{-6}
637(1)[a]	0.10	189	8.4	0.045	6.03×10^{-7}
637(2)		199	5.9	0.070	3.63×10^{-7}
637(3)[b]		210	3.2	0.100	2.25×10^{-5}
637(4)[b]		210	3.9	0.148	5.23×10^{-5}
638(1)	0.05	190	25.6	0.060	1.23×10^{-5}
638(2)		190	18.6	0.089	3.38×10^{-6}
638(3)		190	14.6	0.106	1.36×10^{-6}
638(4)		200	4.8	0.132	2.68×10^{-7}
638(5)		200	10.2	0.153	1.23×10^{-6}
638(6)		200	14.6	0.174	4.51×10^{-6}
638(7)		200	12.6	0.191	2.61×10^{-6}
638(8)		200	18.9	0.214	1.37×10^{-5}
639[c]	0.02, 0	190	23.9	0.260	2.22×10^{-6}
640(1)[b]	0.10	210	4.2	0.062	7.14×10^{-6}
640(2)[b]		200	8.4	0.098	1.53×10^{-7}
640(3)[b]		210	4.2	0.164	4.42×10^{-7}
641(1)[a]		200	5.4	0.059	1.44×10^{-6}
641(2)		200	2.3	0.079	7.15×10^{-8}
641(3)		200	2.1	0.096	5.59×10^{-8}
642(1)	0.10	200	2.4	0.011	4.50×10^{-8}
642(2)		200	3.1	0.022	7.35×10^{-8}
642(3)		200	5.4	0.050	2.12×10^{-7}
642(4)		200	8.6	0.157	6.63×10^{-7}
643(1)	0.02	200	5.6	0.028	8.00×10^{-8}
643(2)		200	8.5	0.061	1.94×10^{-7}
643(3)		200	11.1	0.085	4.43×10^{-7}
643(4)		200	14.4	0.157	1.20×10^{-6}
657(1)	0.02	200	2.9	0.021	6.69×10^{-8}
657(2)		200	3.9	0.044	1.46×10^{-7}
657(3)		200	5.0	0.068	2.51×10^{-7}
657(4)		200	6.4	0.103	3.71×10^{-7}

[a] Misalignment or bending of the specimen during the step; not plotted in Figure 10.
[b] Melt segregation suspected for steps at and following 210 K; not plotted in Figure 10.
[c] Assembly of two vertically-stacked sub-specimens; two χ_{MP6} listed.

Figures

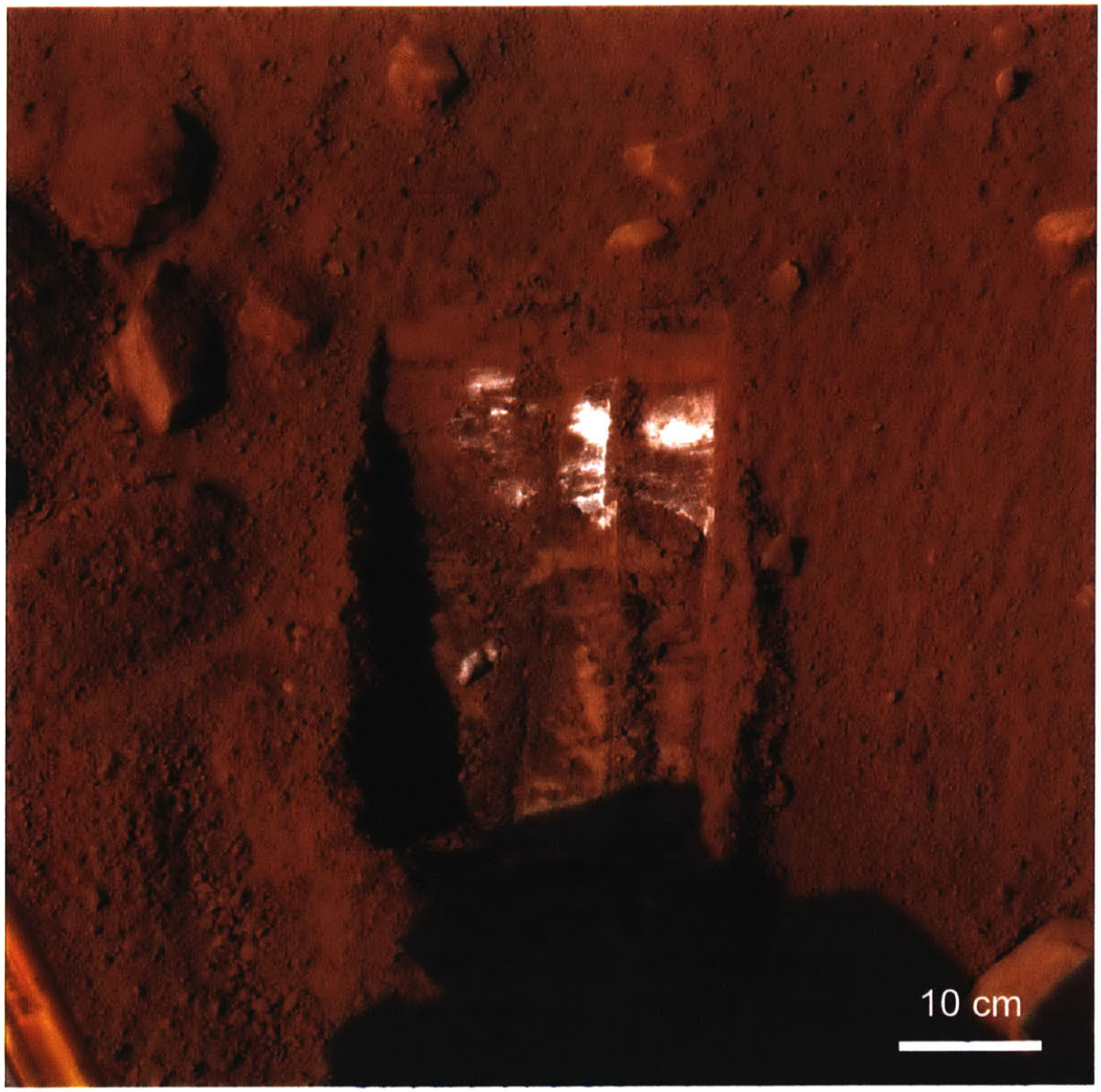

Figure 1. Photograph of the "Dodo-Goldilocks" trench excavated by Phoenix's shovel arm, courtesy of NASA/JPL-Caltech/University of Arizona/Texas A&M University. The Phoenix team discovered a water ice layer several centimeters beneath the soil surface. Soil samples delivered to the onboard Wet Chemistry Laboratory and Thermal and Evolved-Gas Analyzer revealed the presence of 1–2% H_2O and 0.4–0.6% ClO_4^- by mass.

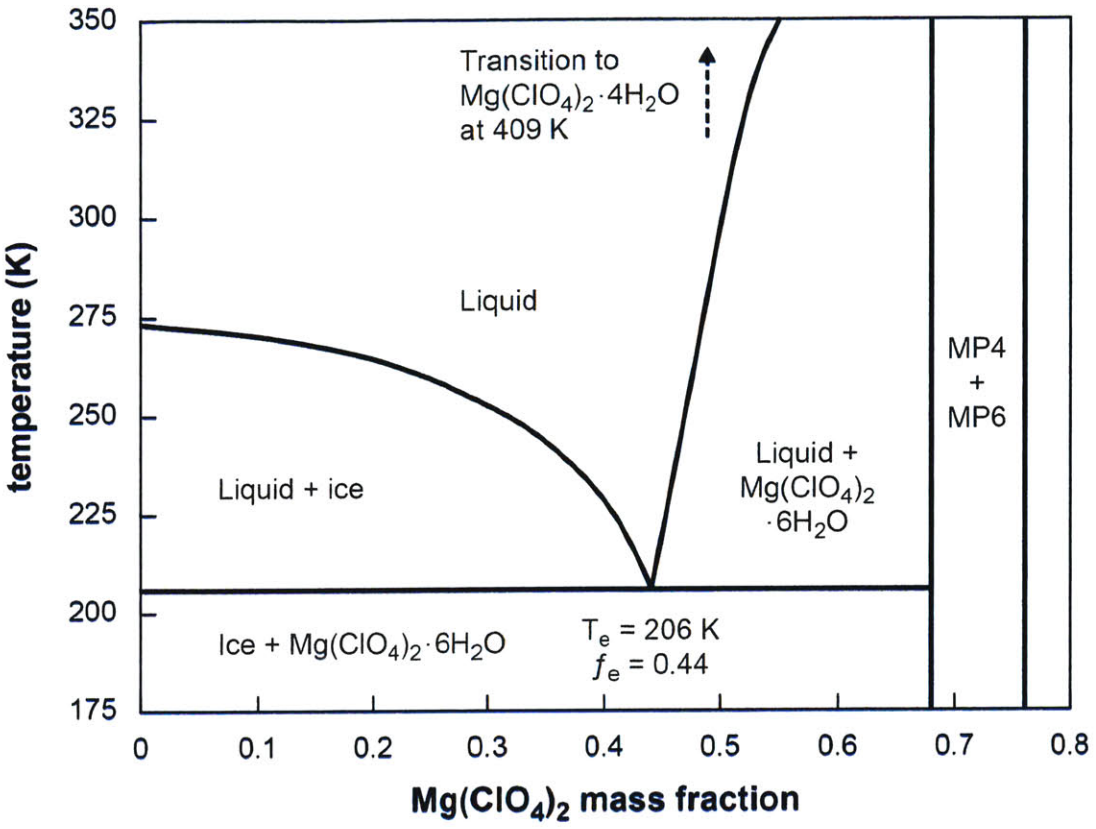

Figure 2. A portion of the phase stability diagram for the H_2O-$Mg(ClO_4)_2$ system (after Chevrier et al., 2009).

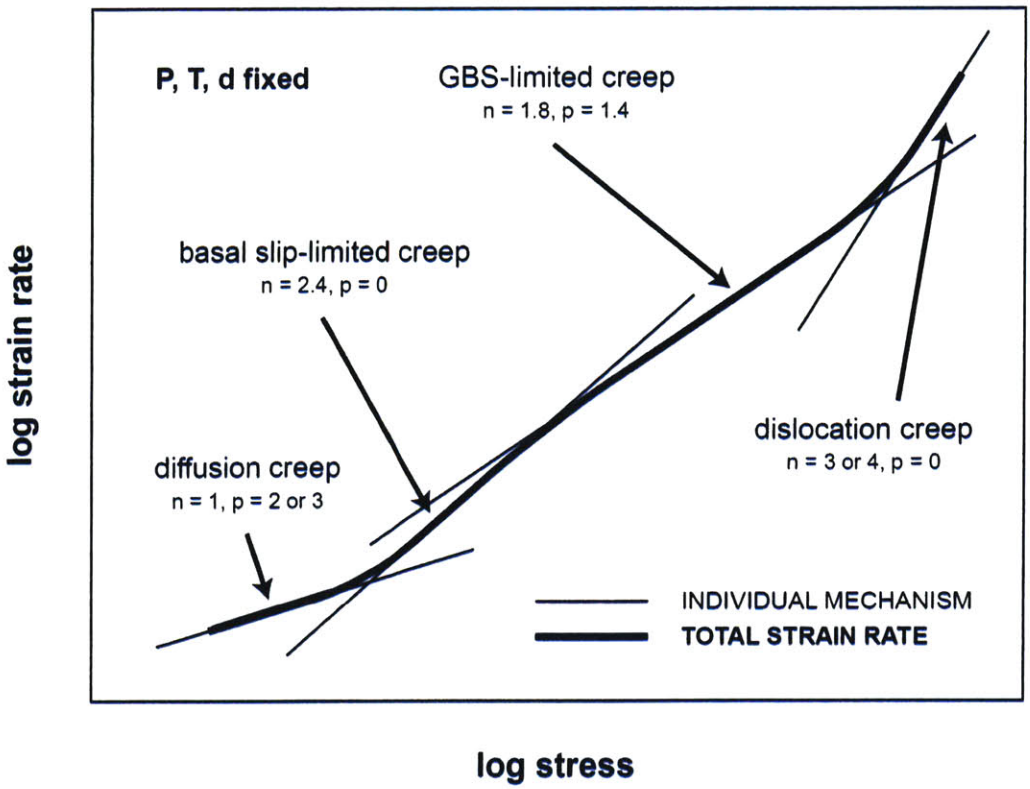

Figure 3. Depiction of the contribution of various ice creep mechanisms as a function of stress (for fixed grain size and temperature) (after Goldsby and Kohlstedt, 2001). Total strain rate (bold line) is approximated as $\dot{\varepsilon}_{\text{tot}} = \dot{\varepsilon}_{\text{diff}} + (\dot{\varepsilon}_{\text{basal}}^{-1} + \dot{\varepsilon}_{\text{GBS}}^{-1})^{-1} + \dot{\varepsilon}_{\text{disl}}$.

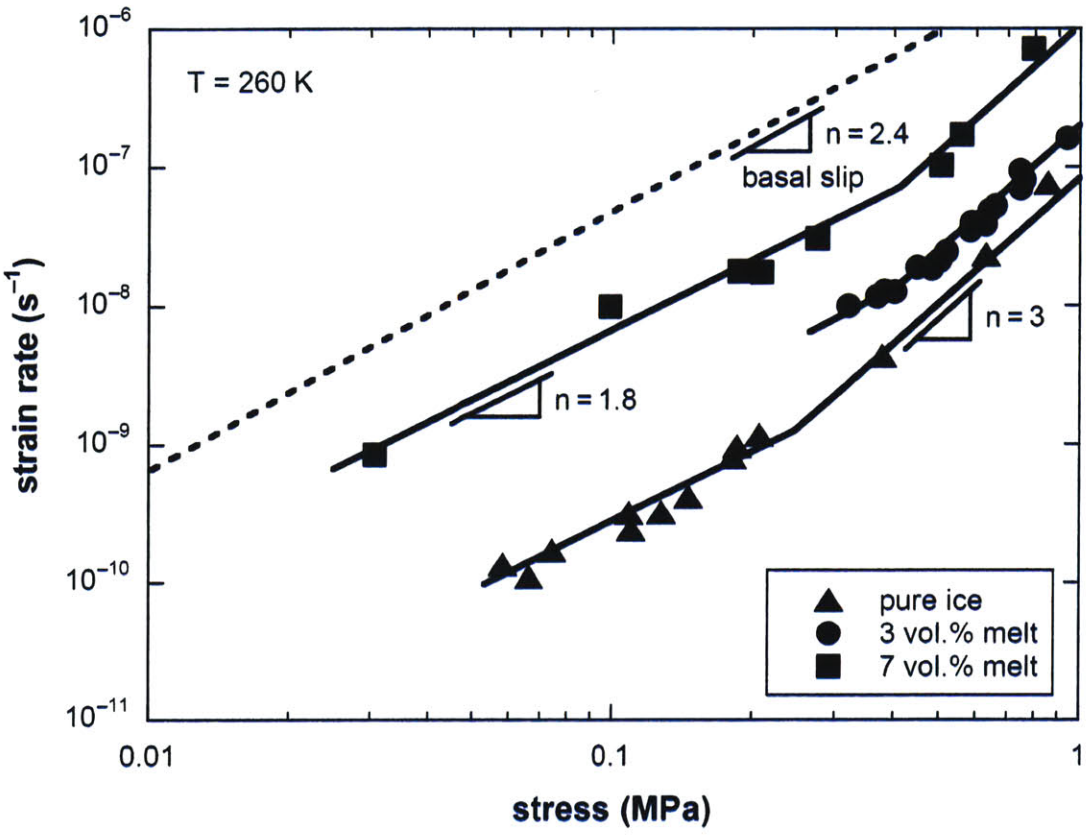

Figure 4. Creep results of partial melts in the H_2O-NaCl system (T_e = 252 K) and pure, polycrystalline ice (grain size of 1.0–3.5 mm for all specimens) (after De La Chapelle et al., 1995). Experiments were performed using a dead-weight apparatus at a confining pressure of 0.1 MPa. Strain rates correspond to steady-state creep obtained after shortening of ~1%.

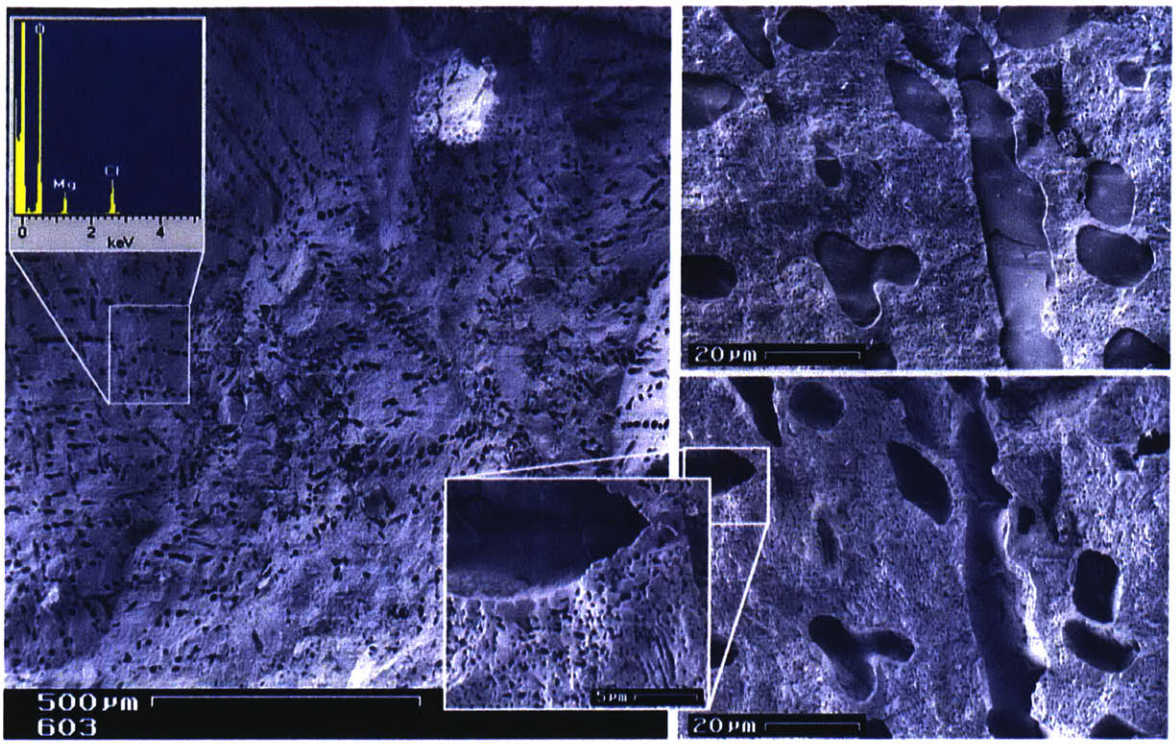

Figure 5. Eutectic ice-MP6 specimen 603. Low-magnification CSEM image at left shows the MP6 phase after most of the ice has sublimated. Here, ice originally occupied the open channels and holes seen along the surface, distributed in a loosely uniform manner and spaced ~50 microns apart. Energy-dispersive X-ray spectroscopy of the remaining solid phase confirms oxygen, magnesium, and chlorine as the only measurable elements (blue box, top left). SEM images at right show a section of specimen after minor sublimation (top) and major sublimation (bottom) of the ice 23 minutes later. Many ice pods are isolated rather than interconnected beneath the surface.

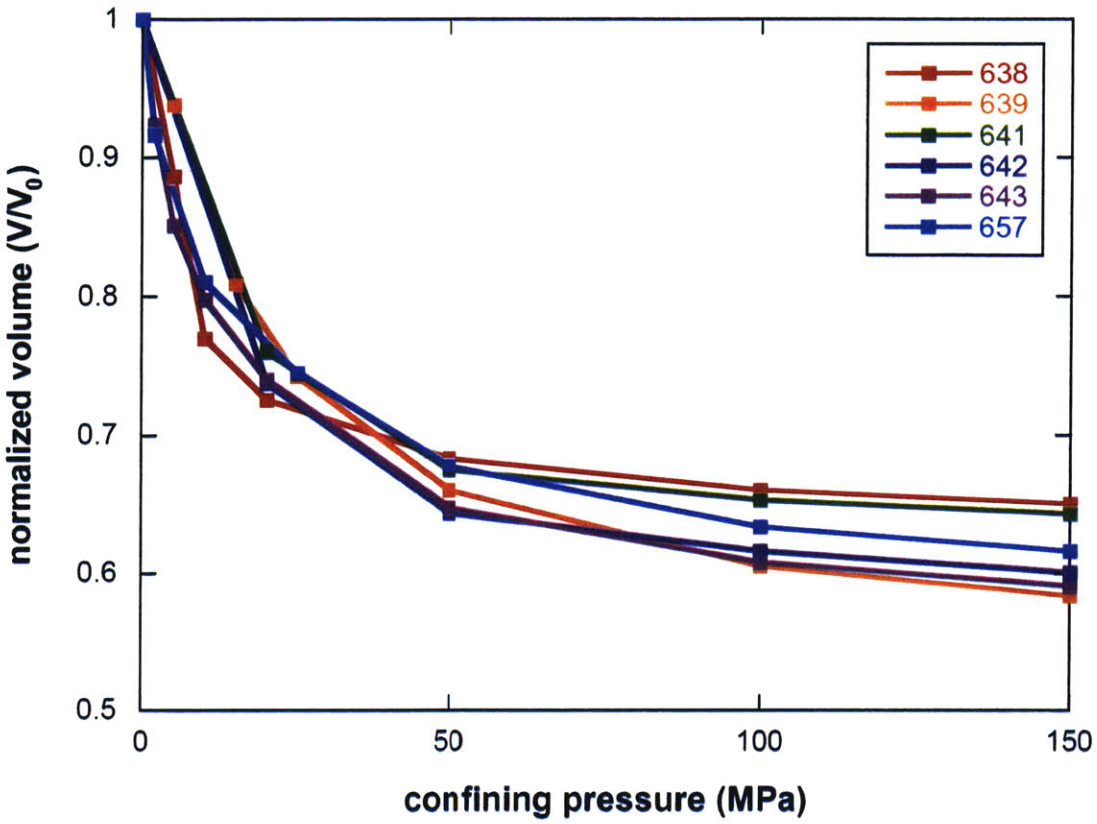

Figure 6. Progress of compaction with increasing confining pressure for various test specimens. Here V_0 is specimen volume before compaction (30–40% pore space) and V is volume at a given confining pressure. The position of the loading piston is used to calculate V (assuming uniform compaction) and an extrapolation to zero pressure for V_0 is required, so uncertainties are accordingly large (±5%).

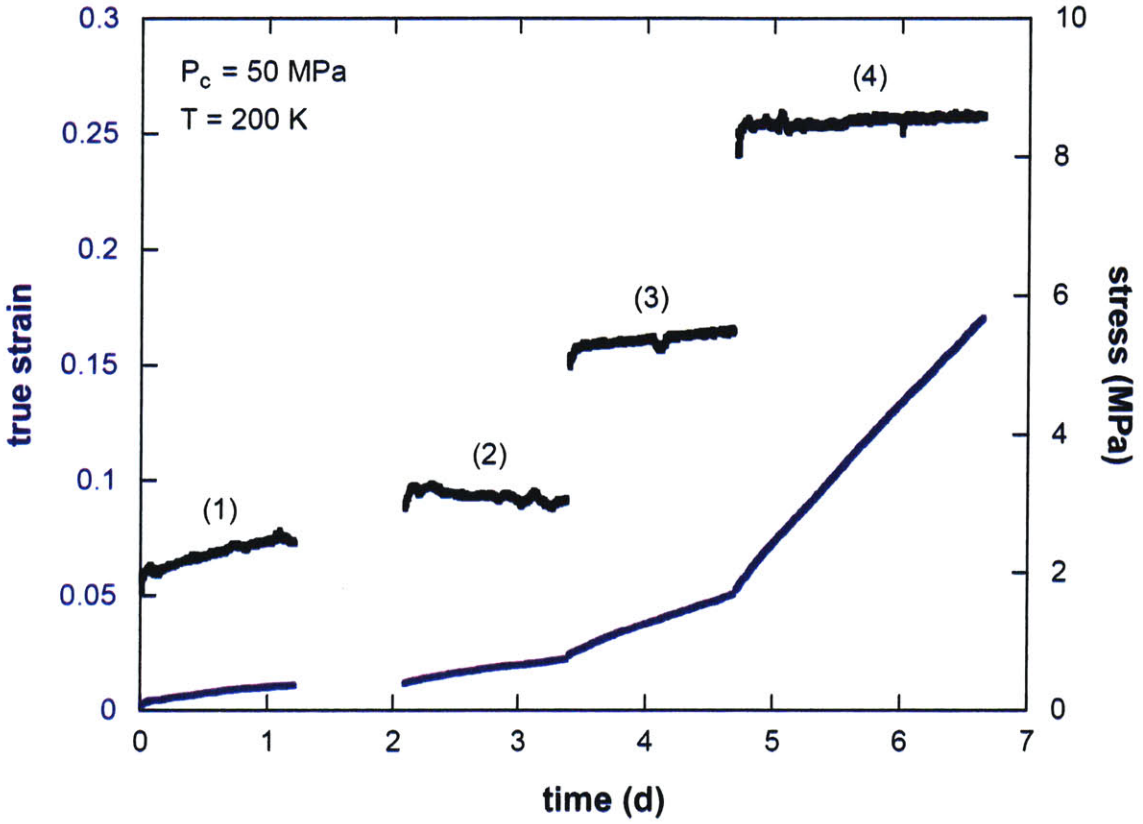

Figure 7. Run record for run 642 showing strain (blue) and differential stress (black) as a function of time. There were four steps in this run at four different (approximately constant) levels of stress. The nonlinear relationship between stress and strain rate ($n \approx 2$ in Equation 1) is apparent.

Figure 8. Specimen 642 ($d \sim 200$ μm and $\chi_{MP6} = 0.10$) following a shortening of ~17%. For scale, the disc upon which the assembly rests has a diameter of 25.4 mm. The specimen occupies the 45-mm length of reduced diameter in the central portion of the assembly. The specimen is bounded top and bottom by steel end caps. All parts are sealed inside a tube of indium metal of wall thickness 0.5 mm, which keeps the gas pressure medium from entering the specimen and assures effective mechanical confinement. A portion of the internal force gauge extends from the top of the assembly.

Figure 9. Specimen 639 after compaction (panel a) and after deformation (panel b). For scale, the disc upon which the assembly rests has a diameter of 25.4 mm. The specimen contains two sub-specimens of similar ice grain size (~200 μm) in series along the stress axis: $\chi_{MP6} = 0.02$ above and $\chi_{MP6} = 0$ below a thin steel disc separating the two (to aid the eye, profiles of the sub-specimens and separating disc are traced out with solid lines). An analysis of shape changes revealed the $\chi_{MP6} = 0.02$ sub-specimen to flow faster than the pure ice by a factor of 1.16 ± 0.04 at identical stress conditions.

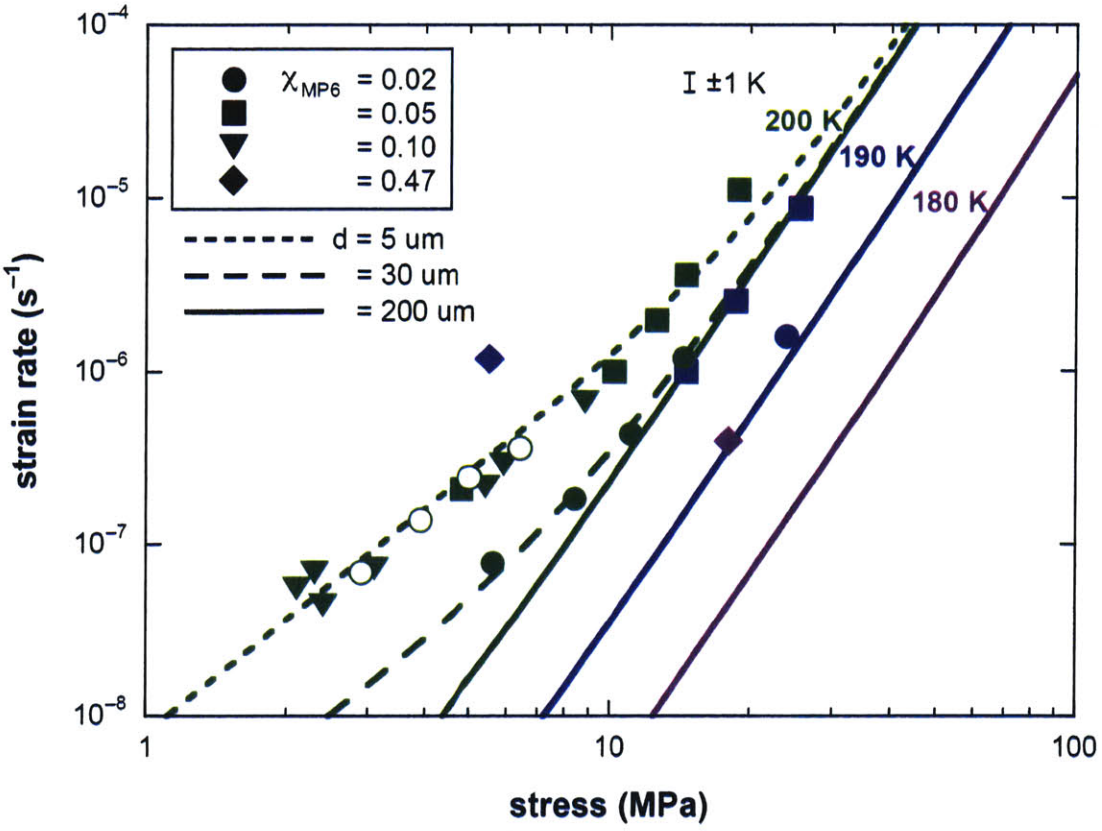

Figure 10. Creep results compared with various grain size and temperature contours (indicated by line style and color) from the calculations of Goldsby and Kohlstedt (2001). All experiments were performed at a confining pressure of 50 MPa. Solid symbols correspond to coarse-grained specimens and open symbols to the fine-grained specimen; symbols follow the same color code as the curves. Measurement uncertainty is approximately equal to the size of the symbols. Not plotted are steps for which the specimen underwent misalignment or bending during deformation, as well as steps at 210 K and for which 210 K had previously been encountered (melt segregation is likely to have occurred).

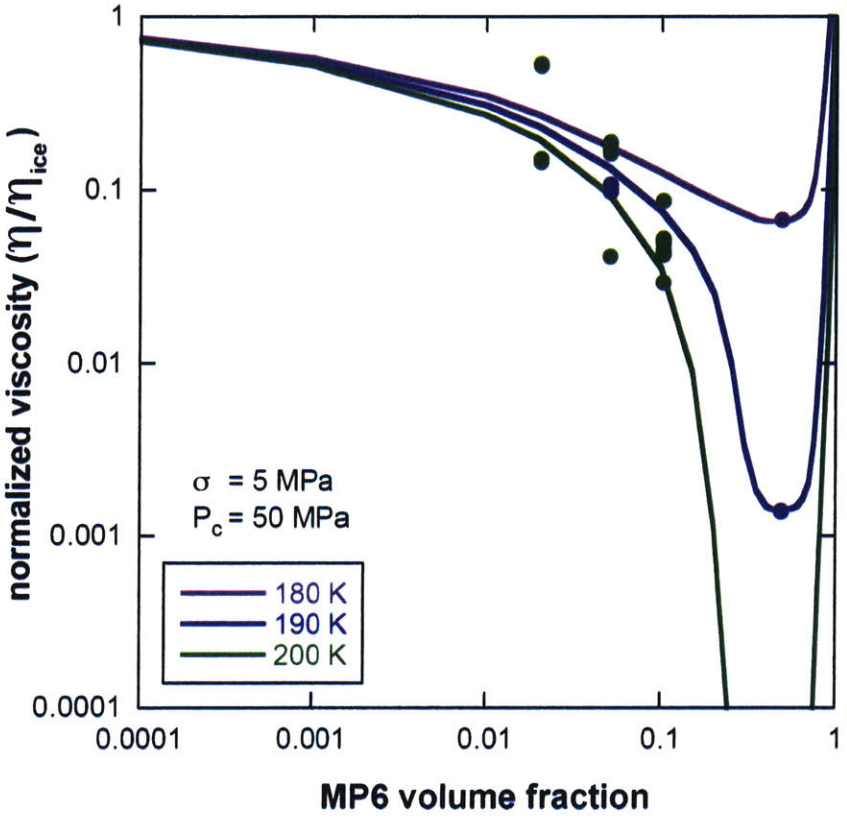

Figure 11. Creep results plotted as dynamic viscosity (normalized to that of pure ice with grain size of 200 μm) vs. MP6 volume fraction in order to make more apparent the weakening effect of MP6. Solid curves are drawn by hand as estimated fits; symbols follow the same color code as the curves. The data are extrapolated as necessary to the 5 MPa value on the basis of $n = 2$ or 4 in Equation 1, depending on the trend in Figure 10. The horizontal axis is logarithmic to bring out detail rather than to imply a physical mechanism.

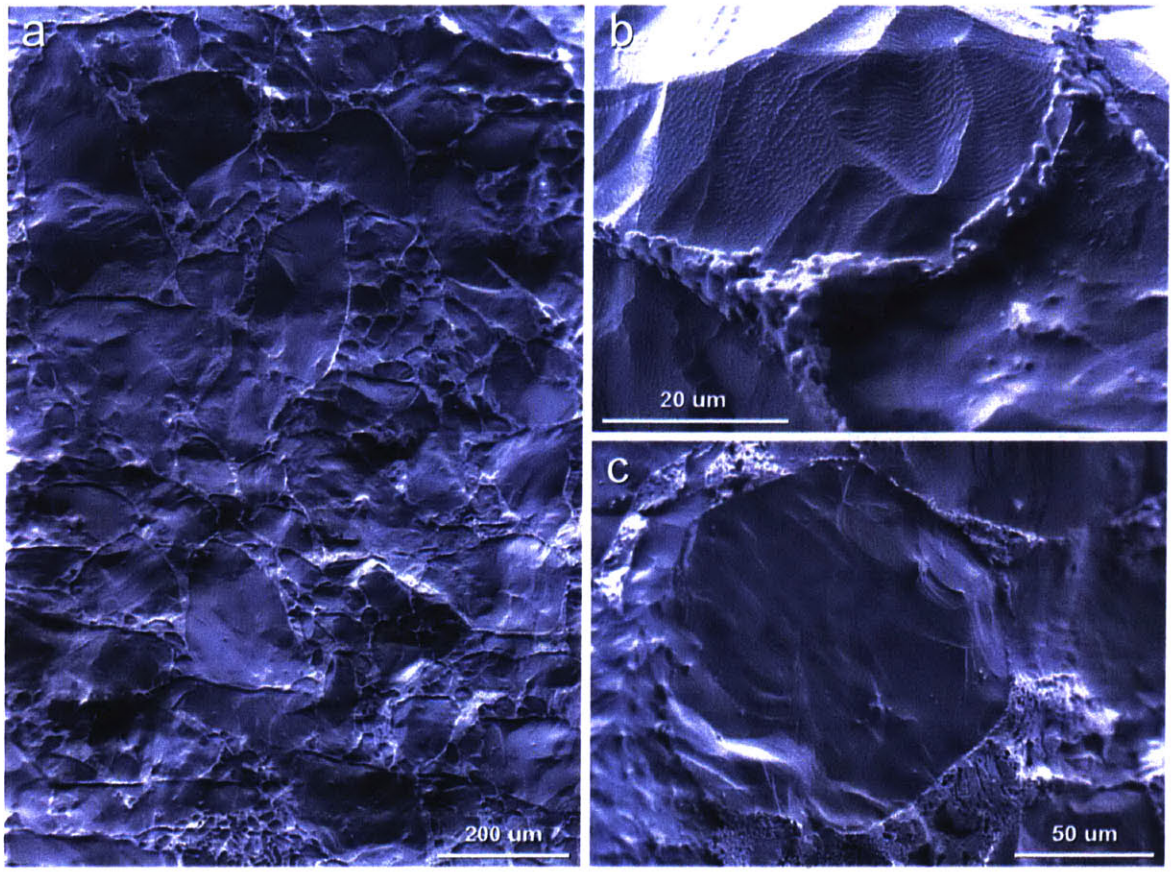

Figure 12. CSEM comparison of two different $\chi_{MP6} = 0.10$ specimens demonstrating the textural uniformity within a single specimen (panel a, specimen 641). Two three-grain junctions from specimen 642 are shown in panel b—here the MP6 phase is the light-colored material standing high in relief relative to the grains of ice that it surrounds. A single ice grain from specimen 642 is enlarged in panel c.

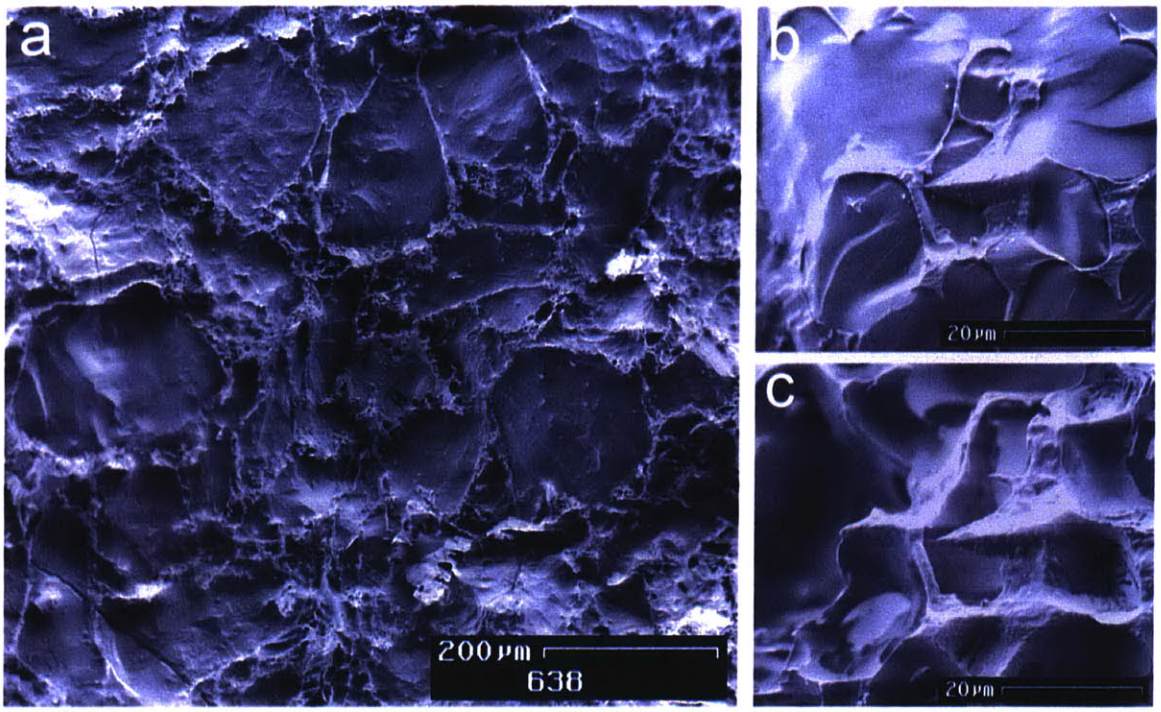

Figure 13. (a) CSEM image of χ_{MP6} = 0.05 specimen 638 showing ice grains uniformly coated by MP6. Despite the lower MP6 content here compared to the specimens shown in Figure 6, the MP6 phase appears quite pronounced due to the time spent in the high-vacuum SEM chamber resulting in significant sublimation of ice. (b, c) A 25-minute time-lapse sequence of an identical section of the specimen, illustrating the dramatic change that accompanies ice sublimation as well as surface deterioration of MP6.

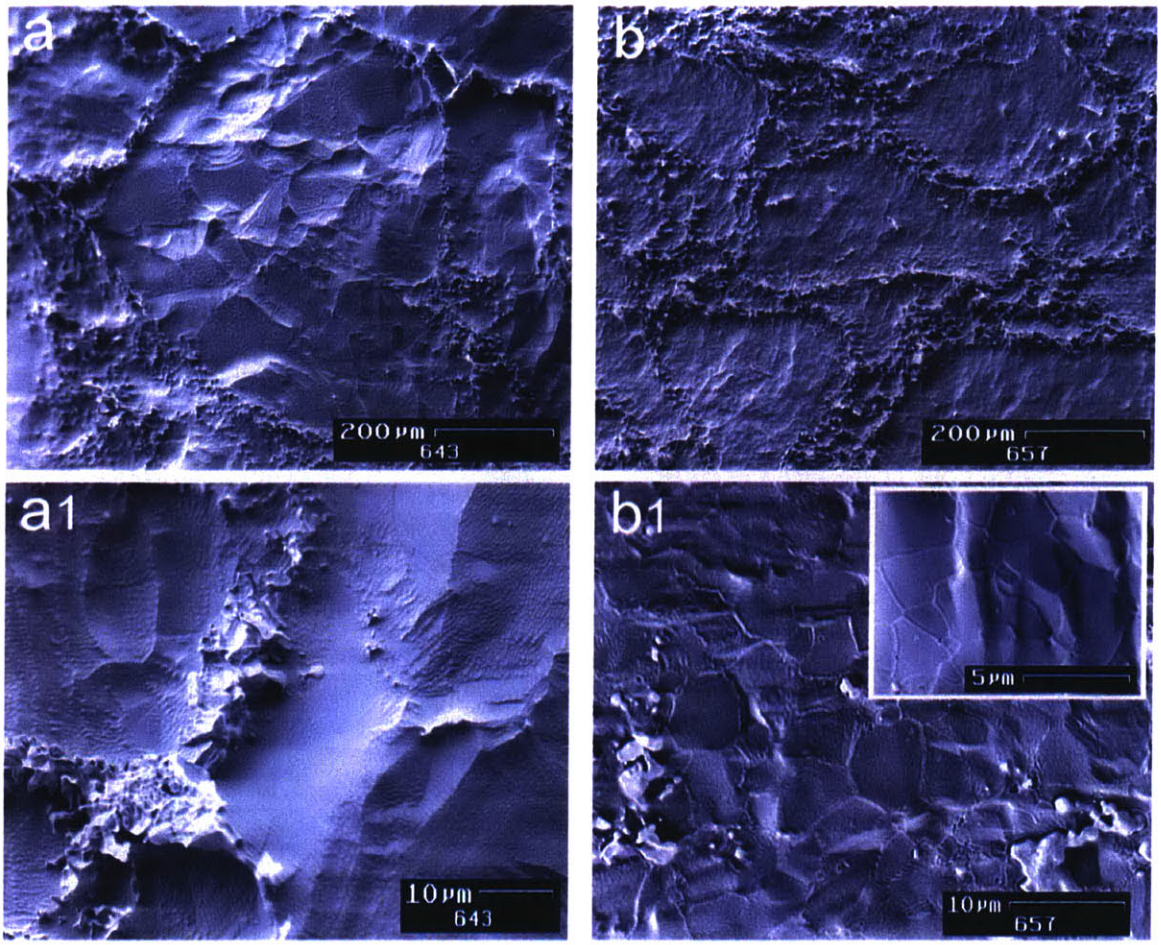

Figure 14. CSEM comparison of χ_{MP6} = 0.02 specimens 643 (made with coarse-grained ice) and 657 (made with fine-grained ice) in panels a and b, respectively. The upper images show low magnification images of the overall specimen structure, and the lower photos (a1, b1) detail ice sections from each specimen. As expected, no ice grain boundaries are visible in 643 (a1) whereas grain boundaries are clearly visible in 657 (b1 and inset). The high-standing MP6 phase in (a1) is at an ice grain boundary, not interior within the ice. In comparison, specimen 657 often exhibits small amounts of MP6 within the ice domains (b1), although many sections of any given domain show ice-on-ice grain contacts with no MP6 (b1 inset). Ice grain size in 657 is fairly uniform at several microns in diameter (b1 and inset).

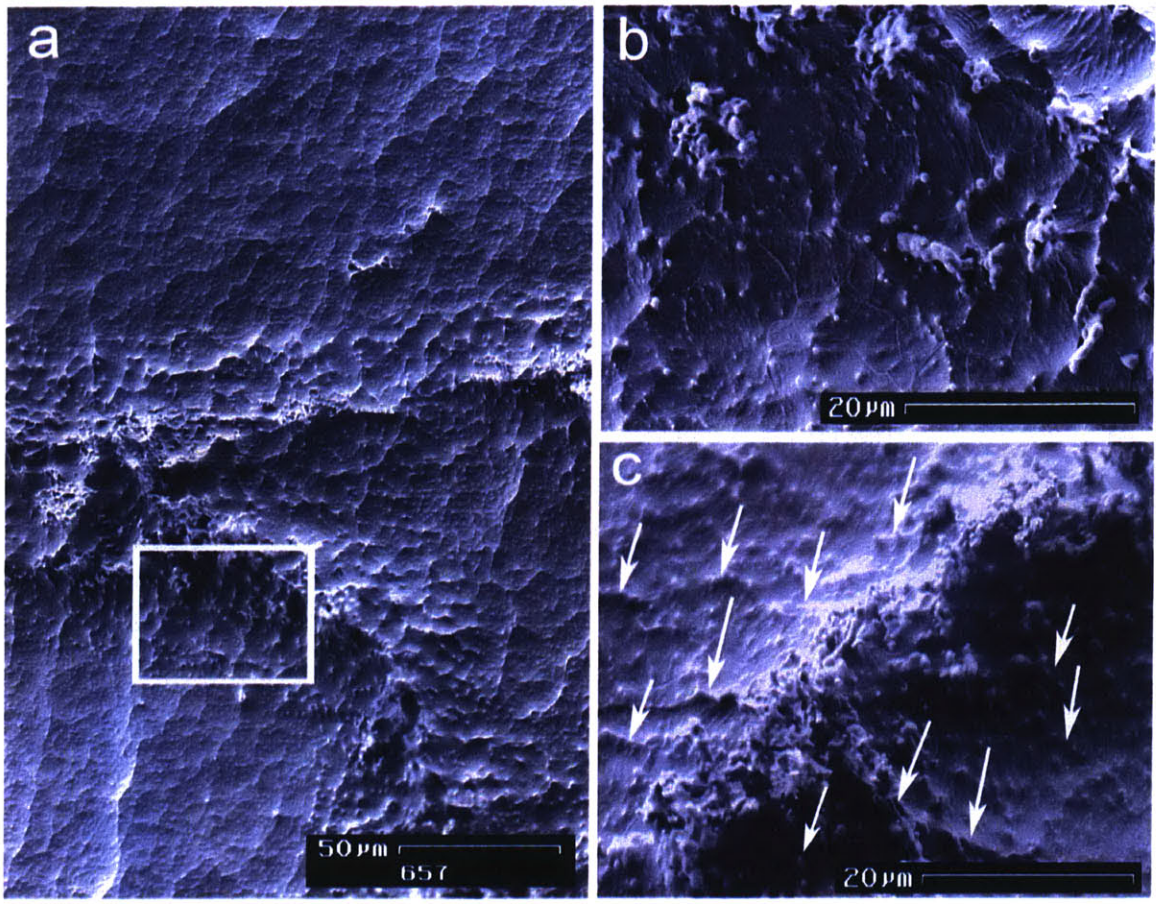

Figure 15. (a) Overview of a domain boundary from the center of specimen 657 (right column) showing apparent migration of MP6 into the fine-grained ice. The clear gradient in MP6 concentration away from the boundary is best seen at this scale. Outlined box in (a) is enlarged in (b), showing ice grain boundaries at several microns in diameter. The MP6 is unstable under extended exposure to the electron beam and tends to collect into the small spheres and clusters of spheres seen here. Virtually all MP6 lies along visible ice grain boundaries. (c) Similar features are visible in a different portion of the specimen, with arrows indicating several areas where MP6 appears to have migrated away from the domain boundary.

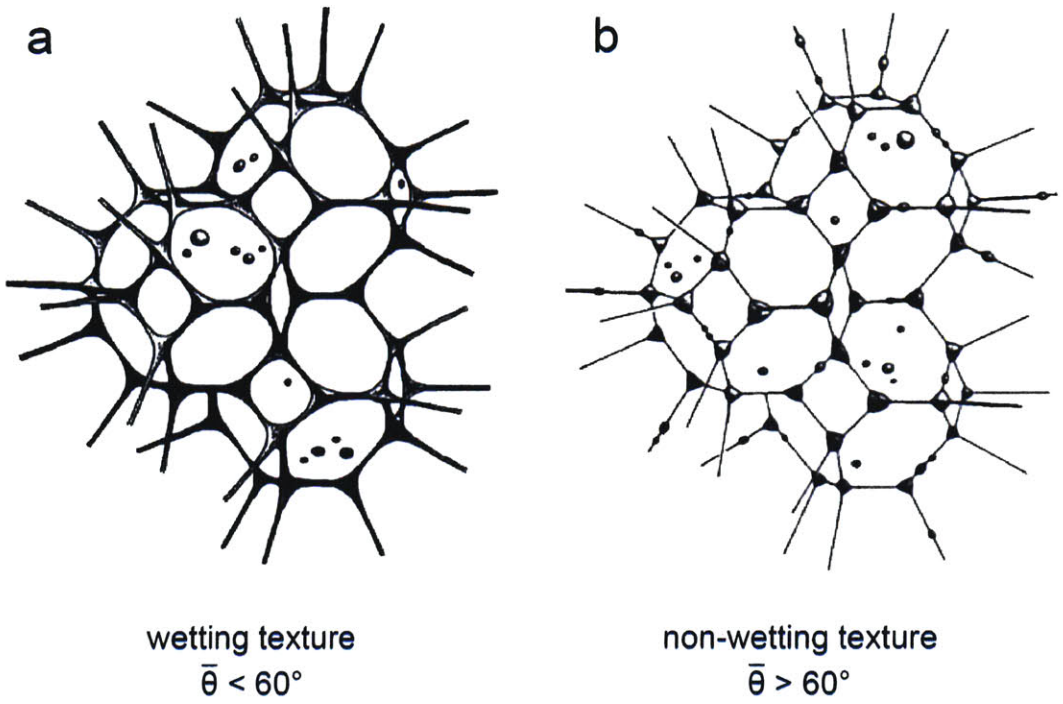

Figure 16. Textures of two-phase systems characterized by the mean dihedral angle ($\bar{\theta}$) between interphase boundaries (after Lee et al., 1991). (a) For $\bar{\theta} < 60°$, the secondary phase is distributed along three-grain junctions of the primary phase, forming an interconnected network between four-grain junctions (wetting texture); for $\bar{\theta} = 0$, the secondary phase is distributed entirely along grain boundaries (complete wetting texture; not illustrated). (b) For $\bar{\theta} > 60°$, the secondary phase is confined to grain boundaries and three- and four-grain junctions in isolated pockets (non-wetting texture).

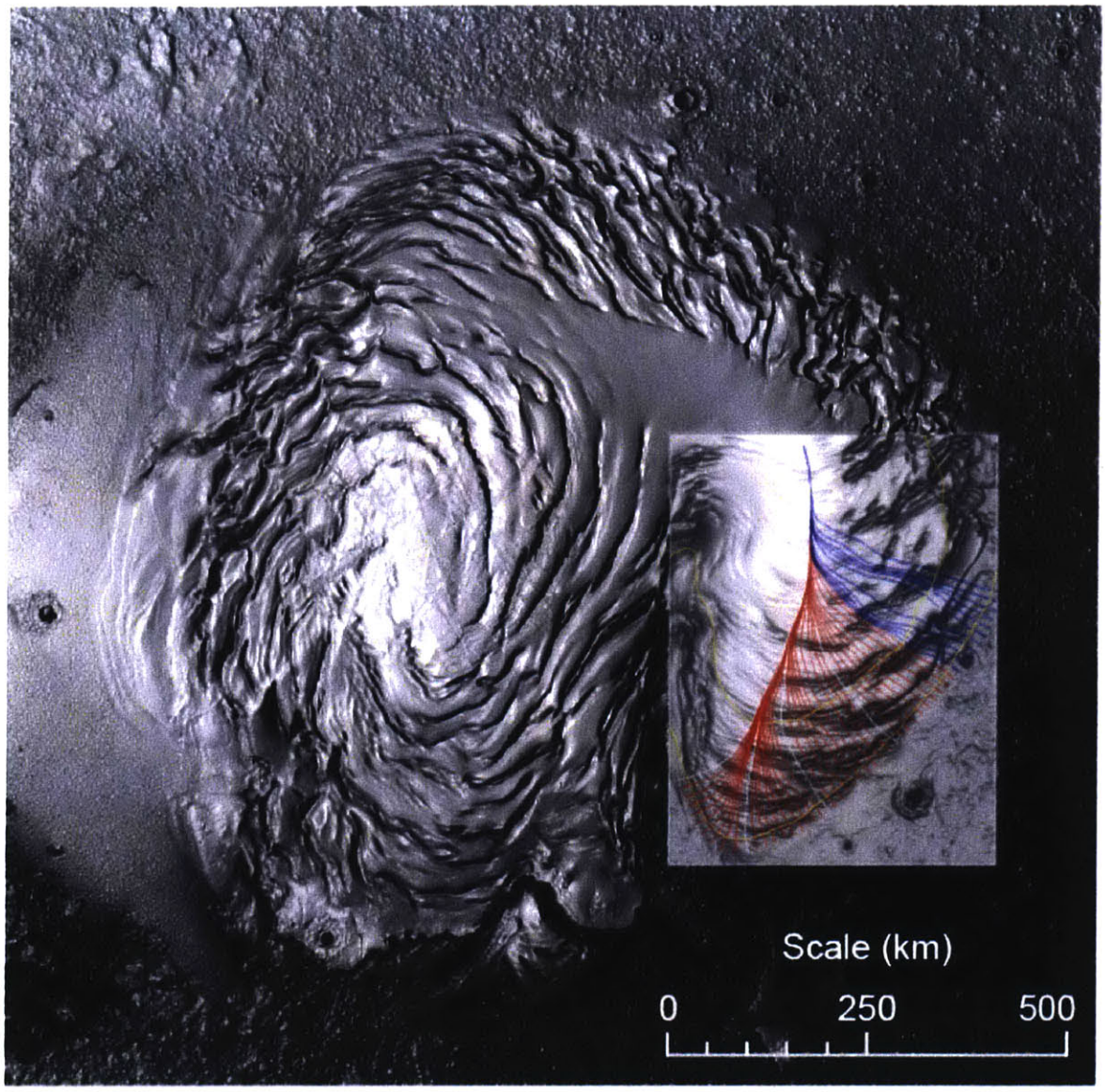

Figure 17. Mars Orbiter Laser Altimeter (MOLA) digital elevation model of the north polar layered deposits. Inset highlights Gemina Lingula with topographic gradient paths analyzed by Winebrenner et al. (2008) (red, white, and blue lines).

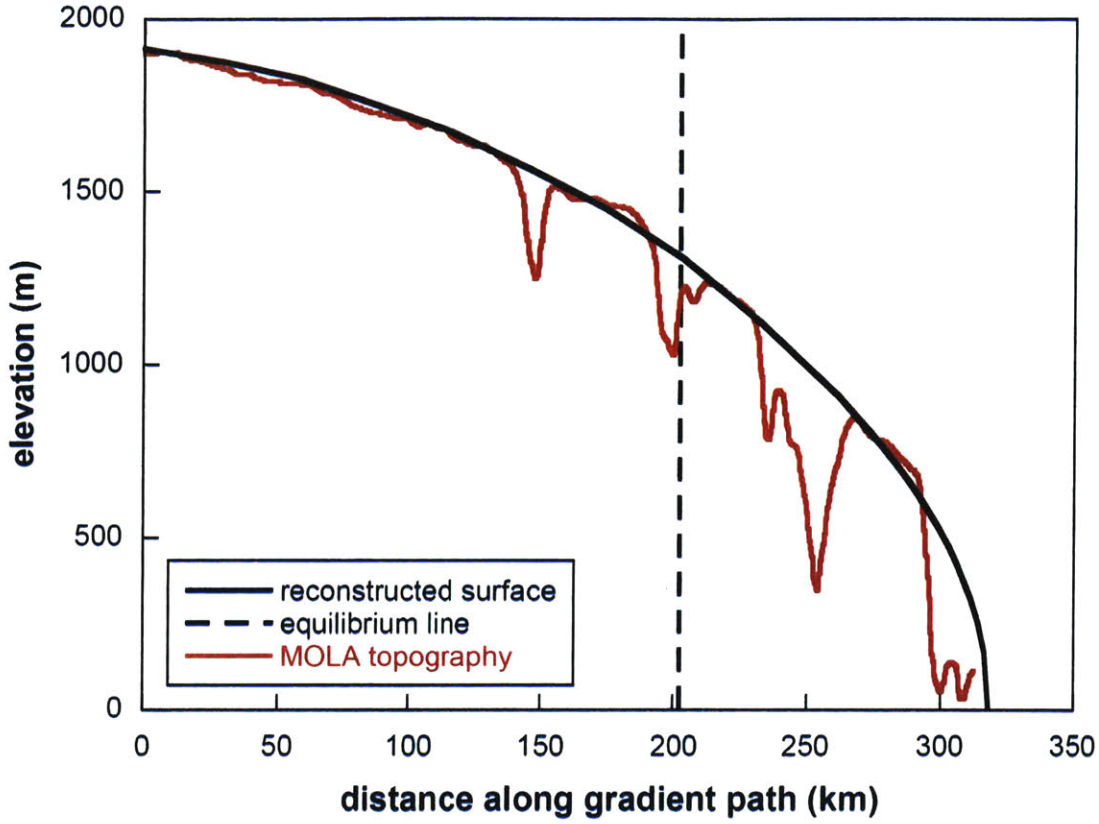

Figure 18. Topographic profile of Gemina Lingula (29th gradient path from left in Figure 17) compared with the shape of a flowing ice mass (after Winebrenner et al., 2008; see Appendix A therein for calculations). Among integral values of n in Equation 1, $n = 3$ provides the best fit to intertrough topography.